(article starts on next page)

Nanomechanical Crystalline AlN Resonators with High Quality Factors for Quantum Optoelectromechanics

Anastasiia Ciers,* Alexander Jung, Joachim Ciers, Laurentius Radit Nindito, Hannes Pfeifer, Armin Dadgar, André Strittmatter, and Witlef Wieczorek*

High-quality factor (Q_m) mechanical resonators are crucial for applications where low noise and long coherence time are required, as mirror suspensions, quantum cavity optomechanical devices, or nanomechanical sensors. Tensile strain in the material enables the use of dissipation dilution and strain engineering techniques, which increase the mechanical quality factor. These techniques have been employed for high-Q_m mechanical resonators made from amorphous materials and, recently, from crystalline materials such as InGaP, SiC, and Si. A strained crystalline film exhibiting substantial piezoelectricity expands the capability of high-Q_m nanomechanical resonators to directly utilize electronic degrees of freedom. In this work, nanomechanical resonators with Q_m up to 2.9×10^7 made from tensile-strained 290 nm-thick AlN are realized. AlN is an epitaxially-grown crystalline material offering strong piezoelectricity. Nanomechanical resonators that exploit dissipation dilution and strain engineering to reach a $Q_m \times f_m$-product approaching 10^{13} Hz at room temperature are demonstrated. A novel resonator geometry is realized, triangline, whose shape follows the Al–N bonds and offers a central pad patterned with a photonic crystal. This allows to reach an optical reflectivity above 80% for efficient coupling to out-of-plane light. The presented results pave the way for quantum optoelectromechanical devices at room temperature based on tensile-strained AlN.

1. Introduction

The engineering of tensile-strained materials has enabled rapid progress in realizing nanomechanical resonators with ever-higher quality factors (Q_m).[1] The low mass and high-quality factor of a nanomechanical resonator result in low thermal force noise, which enables measuring small forces, e.g., required for the detection of single-proton spins[2] or gravity between small masses.[3] Furthermore, a high-$Q_m \times f_m$-product increases the number of coherent oscillations, which is essential for realizing opto- or electromechanical devices[4] for use in quantum technologies.[5]

Nanomechanical resonators with record-high quality factors of 10^{10}[6] have been predominantly achieved in tensile-strained amorphous Si_3N_4, employing dissipation dilution, soft clamping, and strain engineering techniques.[7–11] These techniques have led to a variety of nanomechanical resonator geometries, including 2D phononic crystal (PnC)-shielded membranes,[9] 1D PnC beams,[10] hierarchically-clamped devices,[12] and resonators optimized through machine learning methods.[13,14] Recently, tensile-strained crystalline materials made from InGaP,[15–17] SiC,[18] or Si[19] have been investigated for high-Q_m mechanical resonators. The latter work demonstrated 1D PnC beams in Si with Q_m of 10^{10} at cryogenic temperatures.[19] Crystalline materials have fewer defects, which potentially leads to a larger intrinsic quality factor, and, thus, to an enhanced diluted quality factor. Furthermore, highly ordered materials, depending on their crystal structure, can offer additional functionality, such as electrical conductivity, piezoelectricity, or superconductivity. This would enable interfacing mechanical vibrations directly to electronic degrees of freedom[4,20,21] without requiring the deposition of additional materials on high-Q_m nanomechanical resonators,[22,23] which increases fabrication complexity and may decrease Q_m.[8]

In this work, we demonstrate high-Q_m nanomechanical resonators made from tensile-strained AlN. This crystalline material is non-centrosymmetric, thus, pyro- and piezoelectric, and has so far been utilized in unstrained GHz mechanics.[24,25] Moreover, AlN is widely used in ultraviolet photonics[26,27] and can host defect centers[28] that act as single-photon emitters. AlN is chemically stable[29] and provides a wide bandgap (6.2 eV at 300 K) with a broad transparency window that covers the ultraviolet to mid-infrared range. Hence, AlN is free from two-photon absorption at telecom wavelengths,[30] contrary to Si. These capabilities make

A. Ciers, A. Jung, J. Ciers, L. R. Nindito, H. Pfeifer, W. Wieczorek
Department of Microtechnology and Nanoscience (MC2)
Chalmers University of Technology
Gothenburg SE-412 96, Sweden
E-mail: anastasiia.ciers@chalmers.se; witlef.wieczorek@chalmers.se
A. Dadgar, A. Strittmatter
Institute of Physics
Otto-von-Guericke-University Magdeburg
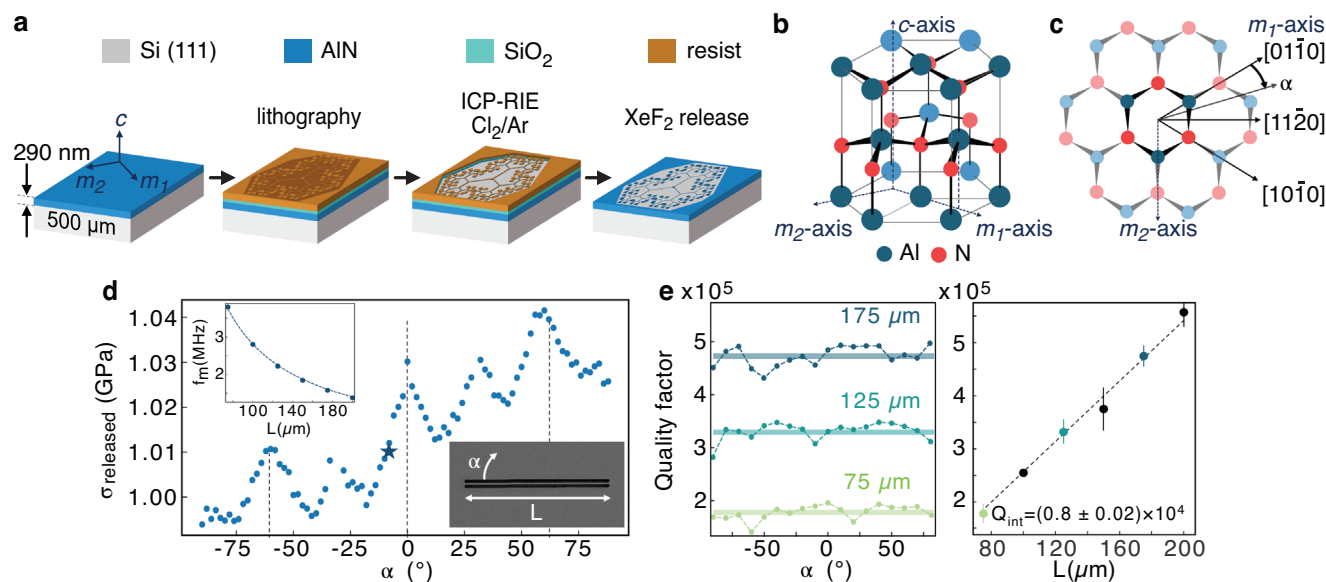39106 Magdeburg, Germany

Figure 1. Material characterization of AlN nanomechanical resonators. a) Illustration of the fabrication process. b) 3D view of the wurtzite AlN crystal, where the m_1 and m_2 axes point along two mirror planes of the crystal, and α denotes the in-plane rotation angle with respect to the m_1-axis. c) Top view of the wurtzite AlN crystal. d) Released in-plane stress, the insets show the fit to Equation 1 for the data-point indicated by the star, and an SEM image of a 175 μm-long beam. e) The mechanical quality factor is largely independent of the in-plane orientation of the beam, α (left), and increases linearly with beam length, L (right). The horizontal lines depict the mean of Q_m (left). The black dashed line is a fit of Q_{int} (right).

AlN and in general III-nitrides suitable materials for realizing a hybrid platform for interfacing electrical, mechanical and optical degrees of freedom.[4]

We realize AlN nanomechanical resonators with Q_m as high as 2.9×10^7 and $Q_m \times f_m$-product close to 10^{13} Hz at room temperature. Mechanical resonators in crystalline III-nitrides have been demonstrated in unstrained AlN[31–34] or compressively strained GaN,[35] but these structures could not profit from dissipation dilution, soft clamping, or strain engineering techniques. Although there are examples of strained AlN resonators,[36] no high-Q_m devices have been reported. In this work, we apply dissipation dilution, soft clamping, and strain engineering techniques to a 290 nm-thick crystalline AlN film of residual tensile stress of 1.4 GPa grown on a Si(111) substrate.[20] We demonstrate high-Q_m nanomechanical resonators with different geometries: uniform beams, tapered 1D PnC beams, and hierarchically-clamped structures. We compare the experimental results with eigenfrequency simulations and dissipation dilution calculations of a prestressed crystalline material with hexagonal symmetry. We present a new resonator type, triangline, whose geometry has three-fold symmetry and follows the Al–N bonds in the crystal structure. Importantly, this hierarchically-clamped triangline provides a central pad that we pattern with a photonic crystal (PhC), which allows us to engineer the pad's out-of-plane optical reflectivity.[37–40]

2. Results

2.1. Fabrication

The fabrication process steps are summarized in **Figure 1a** (details in the Experimental Section and Supporting Information).

The 290 nm-thick wurtzite AlN is grown by metal–organic vapor-phase epitaxy (MOVPE) on a (111)-oriented 500 μm-thick Si wafer. The roughness of the grown film is 1 ± 0.1 nm (root mean square, AFM data in Supporting Information). The resonator geometry is defined by electron-beam lithography. The exposed pattern is then transferred to the underlying AlN layer by ICP-RIE etching with a Cl_2/Ar mixture using a SiO_2 hard mask. Subsequently, the resist and hard mask are removed and in a final step the AlN resonators are released in a dry release step with XeF_2. Such isotropic release allows the pattern to be independent from the substrate orientation, which is not possible with a KOH release etch of Si_3N_4 on a Si(100) wafer,[12] but similar to a dry release etch of amorphous SiC[41] or Si_3N_4[6] on Si. Furthermore, through the dry release process we achieve a high fabrication yield of above 90%. This is contrary to a wet release (e.g., KOH-based), which requires additional lithography, etching steps and critical point drying, to increase the membrane-substrate gap and ensure high fabrication yield for large area resonators.[12] The presented fabrication process allows the realization of a range of high-Q_m nanomechanical resonator geometries including, but not limited to, uniform beams (inset Figure 1d), tapered 1D PnC beams (**Figure 2a**, b), and hierarchically-clamped trianglines (**Figure 3a**).

2.2. Material Characterization

Wurtzite AlN belongs to the P_{6_3mc} space group with a polar axis along the [001] direction, i.e., the c-axis. We illustrate its crystal structure in Figure 1b,c. The AlN crystal has a 19% lattice-mismatch with the silicon substrate underneath,[42] thus, its atoms are displaced from their equilibrium positions
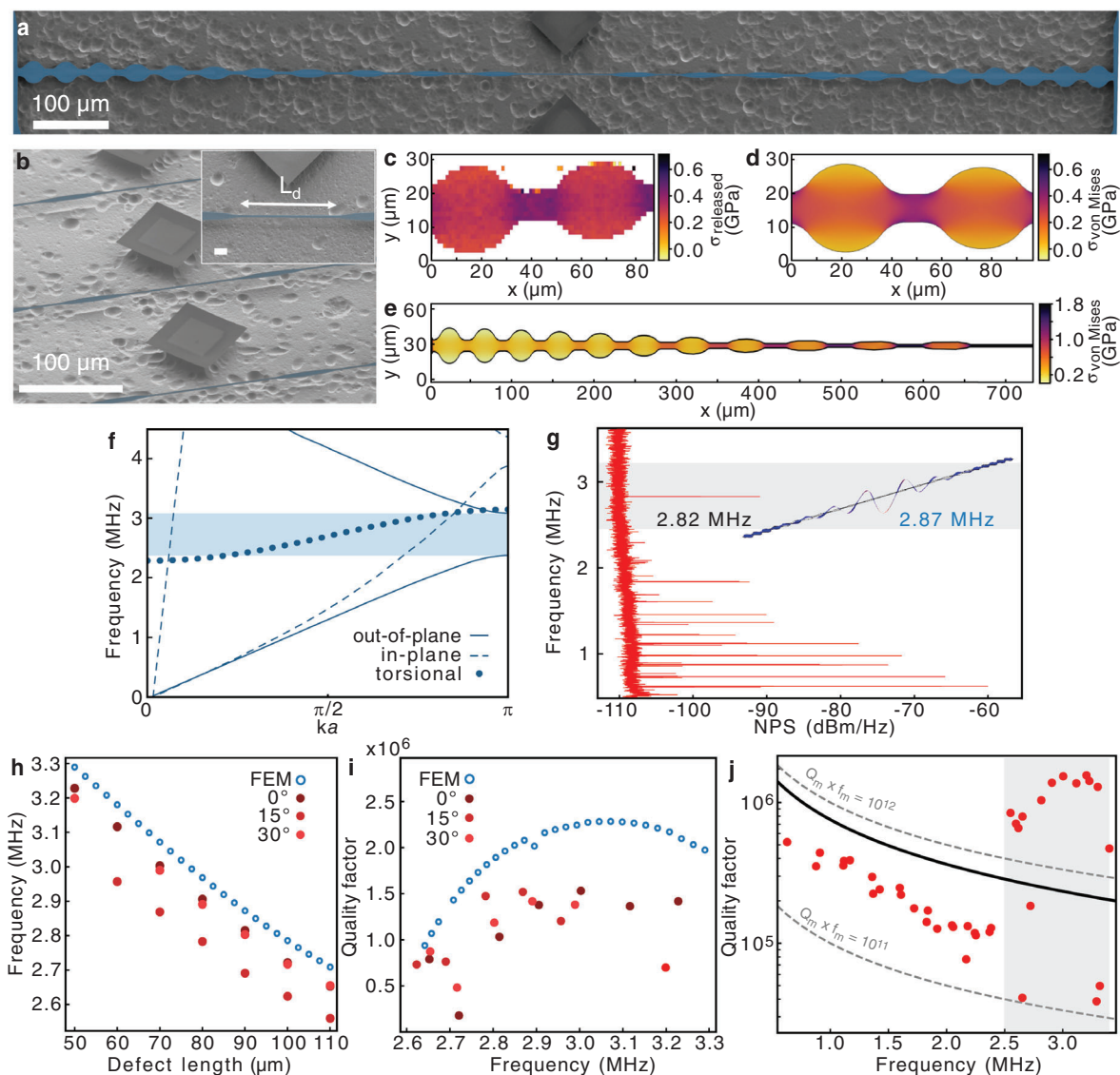
**ADVANCED
SCIENCE NEWS**

www.advancedsciencenews.com

**ADVANCED
MATERIALS**

www.advmat.de

Figure 2. Tapered phononic crystal beams in crystalline AlN. a,b) False-colored SEM images of a 290 nm-thick PnC beam. The inset in (b) shows the PnC defect of length $L_d = 50$ μm (scale bar 10 μm). c) Raman spectroscopy map of a part of the PnC unit cells $i = 9$ and $i = 10$. The colorbar shows $\sigma_{released}$. d,e) FEM simulation results of the stress in the PnC beam for $\sigma_{residual} = 1$ GPa. f) Band diagram of the phononic modes of the $i = 2$ unit cell for $\sigma_{residual} = 1$ GPa. Modes are classified with respect to their transformation under the parity operation (P_y, P_z): (1, −1) (solid lines), (− 1, 1) (dashed lines), and (− 1, −1) (dotted lines), see Supporting Information for more details. g) Representative noise power spectrum (NPS). In the experiment we observe a defect mode at 2.82 MHz, which is close to the FEM simulated value of 2.87 MHz. h) Mode frequency in dependence of defect length and in-plane orientation of the PnC beam. i) Measured and simulated Q_m of the defect mode. j) Measured Q_m versus f_m of PnC beam modes, where defect modes show enhanced Q_m values, larger than uniform beams of similar frequency (solid black line).

resulting in ≈20 nm-thick defect-rich layer at the interface of the AlN film and the Si substrate[43] (TEM images in Supporting Information). The quality of the film improves further away from the substrate,[44] while at the same time introducing a strain gradient.

The AlN film has a thickness of 290 nm and a refractive index of 2.1 in the telecom range, determined via ellipsometry (see Supporting Information). In this work, we do not make use of the piezoelectric properties of the film but have verified that our AlN film is indeed piezoelectric. We determined an effective piezoelectric coefficient $d_{33, \text{eff}}$ of 1.8 pm V^{-1} of the AlN film

rigidly-clamped to the silicon substrate (for details see Supporting Information).

We determine the strain in the AlN film by Raman measurements of the AlN E_2^{high} phonon mode.[45] We observe E_2^{high} at 650.67 cm^{-1}, which corresponds to an average residual stress of the AlN film, $\sigma_{residual}$, of 1.43 ± 0.01 GPa as targeted in the film growth (see Methods Raman Spectroscopy). For simplicity, we assume that the AlN crystal exhibits hexagonal symmetry (for details see Supporting Information), which yields relations for the elastic constants as $C_{11} = C_{22}$, $C_{13} = C_{23}$ and $C_{66} = (C_{11} - C_{12})/2$. Deformations in the c-plane of the hexagonal crystal are then
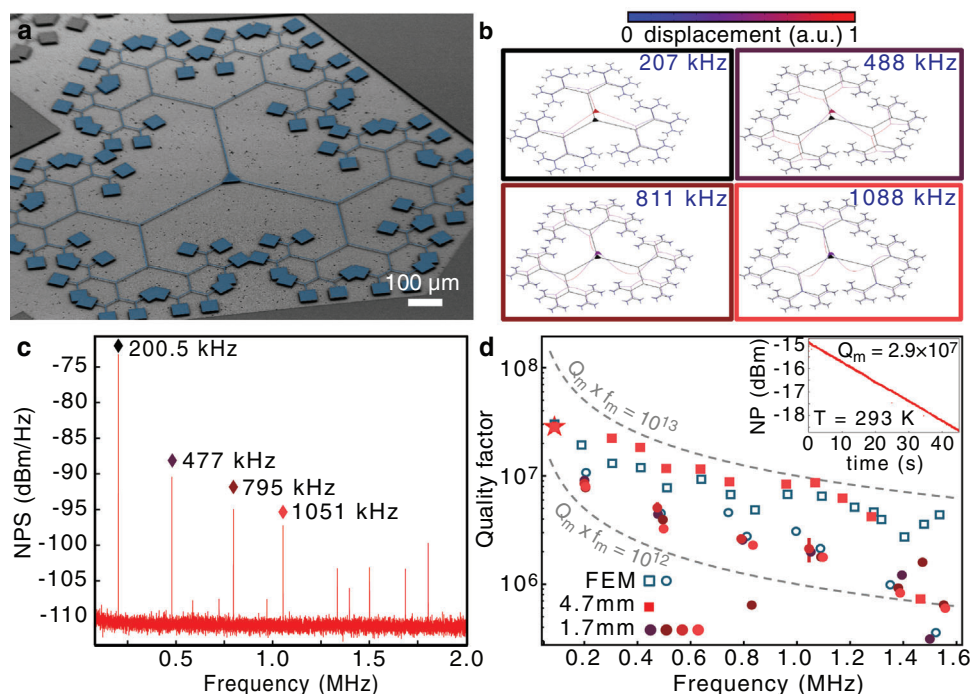
Figure 3. Hierarchically-clamped triangline nanomechanical resonators in crystalline AlN. a) False-colored SEM image of a triangline nanomechanical resonator with a total tether length of 1.7 mm. b) FEM-simulated displacement and eigenfrequency of the first four eigenmodes of the triangline. c) Displacement NPS of the short triangline. The markers show the modes from panel (b). d) Mechanical quality factor versus frequency for different trianglines: dots (squares) are short (long) trianglines. Filled markers are data, open markers are results from FEM simulations. The inset shows a ring-down measurement for the fundamental mode of a long triangline (red star) at 87 kHz.

determined by two elastic constants only,[46] making the model comparable to isotropic materials, like amorphous Si_3N_4.

To measure the released stress and evaluate the intrinsic mechanical quality factor, Q_{int}, we pattern beams of various lengths (75–200 μm) and rotation angles α (−90° to +90°), as illustrated in the inset of Figure 1d. The AlN beams have stress-dominated mechanical frequencies, f_m, with the fundamental mode frequency given as[47]

$$f_m = \frac{1}{2L}\sqrt{\frac{\sigma_{released}}{\rho}} \tag{1}$$

where L is the length of the beam and ρ is the AlN density (parameters in Methods, Table 3). We measured f_m and Q_m of the beams in high vacuum (7×10^{-6} mbar) at room temperature using an optical interferometric position measurement setup (details in Methods Interferometric Characterization Setup). We determined Young's modulus of the AlN film to be $E = 270 \pm 10$ GPa from measurements of the resonant frequencies of higher-order modes of the beam[47] (see Supporting Information). The released stress of the beams extracted from measurements of their fundamental mode frequencies using Equation 1 is shown in Figure 1d. The released stress is close to the expected value of $(1 - \nu)\sigma_{residual} = 1$ GPa (with $\nu = 0.28$ as the Poisson ratio). Instead of a constant released stress expected from a hexagonal symmetry, we observe a weak in-plane anisotropy. We obtain a small periodic stress variation with an amplitude of about 10 MPa. We attribute the 60°-periodicity to the AlN crystal structure[48]

and the additional 30°-periodicity could be the result of crystal twinning[49] (for the discussion see Supporting Information).

The quality factor of a strained high-aspect-ratio mechanical resonator is enhanced by the dilution factor, D_Q, over the intrinsic quality factor, Q_{int}, via[11]

$$Q_D = D_Q \, Q_{int} \tag{2}$$

While Q_{int} is a material property, inversely proportional to the delay between stress and strain, D_Q is engineered by the resonator geometry and depends on the linear and non-linear dynamic contributions to the elastic energy of specific mode shapes (see Methods for the explicit formulae).

We determine Q_{int} from measurements of Q_{beam} of the long, thin strained beams. Their quality factor is limited by dissipation dilution and given as[50]

$$Q_{beam} = D_Q^{beam} Q_{int} \tag{3}$$

with $D_Q^{beam} = \left[(\pi\lambda)^2 + 2\lambda\right]^{-1}$, the stress parameter $\lambda = \frac{h}{L}(12\epsilon_{released})^{-1/2}$, and $\epsilon_{released} = \sigma_{released}/E = 0.0037$ (see more details in Supporting Information). Figure 1e shows Q_{beam} for beams of various lengths and in-plane orientations. We obtain $Q_{int} = (0.80 \pm 0.02) \times 10^4$ for the 290 nm-thick AlN film by fitting the data to Equation 3. We use this value of Q_{int} as input for calculating the expected Q_D of various mechanical resonator geometries from finite element model (FEM) simulations.

2.3. Tapered Phononic Crystal Beams

Strained doubly-clamped beams exploit uniform stress for dissipation dilution, but they exhibit considerable bending at the clamping points leading to mechanical loss. Through the use of soft-clamped resonator designs,[9–11] clamping-related bending losses can be eliminated. A straight-forward approach to implement soft clamping for a beam is to pattern it with a 1D PnC.[10] As a result, the $Q_m \times f_m$-product of a defect mode in a PnC beam increases in comparison with uniform beams of similar frequency (see Figure 2j).

We pattern 1.4 mm-long beams with a PnC. We additionally taper the width of the beam toward the center to co-localize a mechanical defect mode in the region of increased stress, which is a strain engineering method to further increase Q_m.[10] Figure 2a,b shows examples of fabricated devices.

The unit cell of the 1D PnC has a length $a_{PnC} = 90\,\mu m$ at the tapered center and consists of a rectangular-shaped bridge of width $w_{min} = 2\,\mu m$ and an ellipse with a long axis of $a_{PnC}/3$ and short axis $a_{PnC}/27$. The sharp edges at their junction are rounded with a radius of 10 μm. The rounded shapes are essential features as sharp corners that usually characterize these designs would lead to cracking of the highly stressed, brittle AlN film (see Supporting Information for more details). This unit cell is repeated 11 times in both directions from the center defect. We upscale the width of both the bridge (to realize tapering) and ellipse of the unit cells toward the clamping points. The width of the ith iteration of the unit cell, scales as a Gaussian with $w(i) \sim \frac{1}{\beta} - \frac{(1-\beta)}{\beta} e^{-i^2/i_0^2}$ (with $-11 \leqslant i \leqslant 11$ and $i_0 = 7$, $\beta = 0.2$).[10] At the same time we scale the length of the unit cell as $a_{PnC}(i) \sim 1/\sqrt{w(i)}$ to adapt the bandgap of each cell to the frequency of the defect mode.[10]

Figure 2f shows the band diagram for the $i = 2$ unit cell (Supporting Information shows band diagrams of additional unit cells). We can classify the mechanical modes in this band diagram with regards to their parity under transformations P_l where $l = x, y, z$, for example, $P_x(x', y', z')^T = (-x', y', z')^T$. Such transformations applied to the displacement vector $\mathbf{u}$ yield, for example, $P_x\mathbf{u}(x, y, z) = (P_x\mathbf{u})(P_x(x, y, z)) = \pm\mathbf{u}(-x, y, z)$.[51] We observe a bandgap between 2.5 and 3 MHz for out-of-plane modes with $(P_y, P_z) = (1, -1)$ symmetry. In-plane $(-1, 1)$ and torsional $(-1, -1)$ modes cross this bandgap, but these modes do not couple to the out-of-plane motion due to symmetry (see Supporting Information for the simulated displacement of the modes and a description of their transformation under parity operations).[52]

The defect is formed at the middle of the PnC beam through the insertion of an additional bridge of length L_d between the unit cells, see Figure 2b, such that the defect mode frequency is within the effective bandgap.[10] This allows for soft-clamping of the defect mode and, at the same time, focuses the stress through the tapering of the bridges at the center. We perform Raman measurements of a fabricated PnC beam to assess its stress distribution. Figure 2c shows results for two unit cells near the clamping point. We observe a good match between the FEM simulated and measured $\sigma_{released}$ and f_m of the PnC beam for $\sigma_{residual, FEM} = 1$ GPa, Figure 2c,d,h. The measured residual stress of the unreleased AlN film next to the PnC is, however, the same as on other samples, i.e., $\sigma_{residual} = 1.4$ GPa (inferred from Raman measurements). The discrepancy between the measured residual stress, $\sigma_{residual}$, and the FEM assumed $\sigma_{residual, FEM}$ may be the result of

inhomogeneous strain distribution of the AlN film, leading to partial stress relaxation and buckling of the ellipse regions in the PnC beam, thus, reducing locally its stress (see Supporting Information).

Figure 2g shows a thermal noise displacement power spectrum (NPS) of a PnC beam with $L_d = 90\,\mu m$. The defect mode is clearly visible at $f_m = 2.82$ MHz, which is very close to the value obtained from FEM simulations. We summarize measurements of the defect mode frequency for PnC beams of different defect mode lengths and in-plane orientation in Figure 2h (NPS of several beams are shown in Supporting Information). The frequency of the defect mode decreases with increasing defect length L_d, as expected from the FEM simulations, and is close to the simulated value. Furthermore, the defect mode frequency for the beam at 0° orientation and 30° are similar, while at 15° f_m is lower, see Figure 2h. This observation is consistent with the in-plane angular dependence of $\sigma_{released}$ of the uniform beams (Figure 1d). Figure 2i shows Q_m of the defect modes. We observe no systematic change in the quality factor with beam orientation, similar to the in-plane rotated uniform beams (Figure 1e). While the trend of the measured Q_m versus defect mode frequency follows the trend of the FEM simulations, the absolute value of the measured data is slightly smaller than the FEM simulated one. This difference may be the result of buckling of the ellipses and fabrication imperfections (see Supporting Information), breaking the symmetry of localized defect modes and leading to mechanical dissipation through radiation loss into modes of other symmetry.

Figure 2j shows Q_m of delocalized and localized modes of the PnC beams. We observe that mechanical modes within the defect mode frequency range of 2.5 MHz to 3.5 MHz exhibit an enhanced $Q_m \times f_m$-product. We reach a maximal $Q_m \times f_m$-product of up to $4.5 \cdot 10^{12}$ Hz, which is larger than the one of uniform beams of similar frequency (solid line in Figure 2j). This confirms the soft clamping of the defect mode through the strain-engineered PnC.

2.4. Hierarchically-Clamped Triangline Resonators

Optomechanical experiments with a Fabry-Pérot-type cavity require efficient and lossless coupling of a mechanical resonator's out-of-plane displacement to an optical beam. A mechanical resonator should then provide a non-absorbing, out-of-plane oscillating part with a sufficiently large area for accommodating an optical beam. This can be realized, for example, with trampoline-like resonators.[17,53,54] To increase their Q_m, a type of soft clamping based on hierarchical structures can be applied.[55] That has been demonstrated in Si_3N_4-based hierarchically-clamped trampolines[12] and trampoline-like geometries found by machine learning.[14] Further, the trampoline geometry typically realizes a high-Q_m for its fundamental mode, which is advantageous to use in certain quantum optomechanics protocols when nonlinear noise processes, such as thermal intermodulation noise,[56] should be minimized. Finally, the central pad of a trampoline can be patterned with a PhC allowing to engineer its out-of-plane reflectivity.[17,37,53]

A hierarchically-clamped trampoline consists of a central pad that is connected to four beams of length l_0. Each of these beams branches with an angle θ into two subsequent segments, with N

such branching iterations in total toward the clamping points.[55] The length of subsequent segments ($1 \leqslant n \leqslant N$) is $l_n = l_0 r_l^n$ with $r_l < 1$ and segment width $w = w_0 (1/2\cos(\theta))^n$ to maintain a uniform stress in the structure.[55]

We first studied the effect of the branching angle on the $Q_m \times f_m$-product of uniform-width beams in the crystalline AlN film. To this end, we fabricated beams with $N = 1$ branching iteration and varied their branching angle θ (see Supporting Information). We find that $\theta = 60°$ yields singly-branched beams with a large $Q_m \times f_m$-product. At the same time, a geometry with this branching angle follows the in-plane crystal structure of AlN, advantageous for achieving homogeneous stress along all directions of the branched tethers, resulting in uniform stress in all branched segments.[55]

To follow the in-plane 120° rotation symmetry of the crystal, we use a triangular-shaped central pad that is suspended with three tethers. Each of the tethers branches off N times at $\theta = 60°$ into two segments (see Figure 3a). We call this geometry triangline. When comparing this triangline with a hierarchically-clamped trampoline, we find that the expected f_m and Q_m of these two structures are very similar (see Supporting Information). An important advantage of the triangline geometry is that it enables a more economic use of the chip area, which allows us to increase the number of total branching iterations, and, thus, results in a larger Q_m.

We fabricated two generations of trianglines that differ in their branching iterations N and initial beam lengths l_0. Both generations have a central pad that is patterned with a PhC and has a side-length of 60 μm. The pad is held by beams of constant width $w_0 = 2$ μm and $r_l = 0.63$. We round the sharp edges of the triangline with a radius of 15 μm to avoid cracking during fabrication. The first generation of trianglines, denoted as short, has $N = 5$ branching iterations and an initial beam length of $l_0 = 0.32$mm. This yields a total tether-length between furthest clamping points of 1.7 mm. We simulate the first four eigenmodes and eigenfrequencies of this triangline, which are shown in Figure 3b. The eigenfrequencies experimentally inferred from the measured thermal noise displacement power spectrum (Figure 3c) agree with FEM simulation results. We measured f_m and Q_m of four devices and show the results in Figure 3d. For the fundamental mode of the short triangline we find $f_m = 200$kHz with $Q_m = 9.4 \times 10^6$, yielding a $Q_m \times f_m$-product of 1.9×10^{12} Hz. We find that the FEM-predicted f_m and Q_m are in a good agreement with the measured values. Hence, we conclude that Q_m is limited by intrinsic dissipation (gas damping is not limiting dissipation mechanism, see measurements in Supporting Information).

To increase Q_m, we fabricate a second generation of trianglines, which we denote as long, with one more branching iteration, i.e., $N = 6$, and a longer initial beam length, $l_0 = 0.9$mm, resulting in a total tether length of 4.7 mm between furthest clamping points (see Supporting Information). This triangline exploits to the best of our knowledge the largest number of branching iterations demonstrated to date for trampoline-like hierarchically-clamped resonators.[12] The longer tether length lowers the fundamental mode eigenfrequency to 87 kHz while Q_m improves up to 2.9×10^7 (inset of Figure 3d), yielding a $Q_m \times f_m$-product of 2.5×10^{12} Hz, which is 30% larger than for the fundamental mode of the short triangline. For higher order modes, the $Q_m \times f_m$-product reaches 10^{13} Hz, entering the regime of coherent oscillations for

quantum optomechanics experiments at room temperature (required $Q_m \times f_m > 6 \times 10^{12}$ Hz[57]). We find a good agreement between FEM simulated and experimentally observed f_m and Q_m (Figure 3d).

The optical reflectivity of an unpatterned AlN film is determined by its thickness and refractive index. For the 290 nm-thick AlN film at a wavelength of 1550 nm the reflectivity is below 25% (see **Figure 4**). To increase it, we pattern the central pad of the triangline with a PhC,[37,40] as shown in Figure 4. We pattern a hexagonal PhC with lattice constant $a_{PhC} = 1450$nm and hole radius $r_{PhC} = 508$nm into the AlN film to maximize its reflection of a normally-incident Gaussian beam at a wavelength of 1550 nm. The PhC parameters were obtained from simulations of the suspended film's reflectivity using rigorous coupled-wave analysis (RCWA)[58] (see Supporting Information). Note that the electro-optic effect in AlN could be used to in-situ tune the optical reflectivity with about a few picometers per volt, see Supporting Information.

We patterned first a fully-clamped circular 180 μm diameter AlN membrane with a PhC and observe that its reflectance is increased to above 90%, see Figure 4. The circular clamping guarantees a uniform connection of the membrane to its support, but lowers Q_m, see **Table 1**. We observe pronounced reflectivity dips at 1510 nm and 1580 nm. The first apparent dip originates from the Fano shape of the PhC reflectance. The second dip can be reproduced by RCWA simulations of the patterned 290 nm-thick AlN film with an incident Gaussian beam of 6.4 μm waist. We thus identify the dip at 1580 nm as coupling of the beam into a PhC guided resonance.[38] In the Supporting Information we show reflectance measurements with varying optical waist that let us clearly identify the guided resonance. Further, these measurements demonstrate that we can achieve a reflectance above 99% when using a beam waist of 16 μm. We then patterned a PhC into the triangline's central pad and observe that its reflectance reaches a value above 80% at 1545 nm. Thus, the reflectance of the triangline's pad is drastically increased over the AlN film's reflectivity, but is slightly lower than the reflectance of the PhC-patterned circular membrane. The radius of the PhC holes of the triangline and the circular membrane differs by 6 nm. This causes a small shift of the overall Fano resonance to longer wavelengths. As a result, the PhC guided resonance appears now at 1585 nm and the minimum of the Fano resonance at 1515 nm. We also observe a reflectivity dip at 1558 nm. We identify this dip as the formation of an approximately 3.7 μm-long low-finesse cavity between the PhC and the rough silicon substrate underneath. The overall lower reflectivity compared to the circular PhC membrane may be the result of the low-finesse cavity and the finiteness of the PhC lattice on the pad, which both influence the pad's reflectivity. The reflectivity of the triangline's PhC pad could be improved by using a larger pad size to minimize finite-size effects. The triangline nanomechanical resonator could be integrated into a free-space optical cavity when incorporating some additional fabrication steps. For instance, one could introduce an AlInN/GaN-based distributed Bragg reflector and a sacrificial layer of GaN below the current AlN device layer during the growth. This would realize an optomechanical microcavity, similar to Ref. [59]. Alternatively, one could back-etch the Si substrate of the current devices to place the triangline nanomechanical resonator directly inside an optical
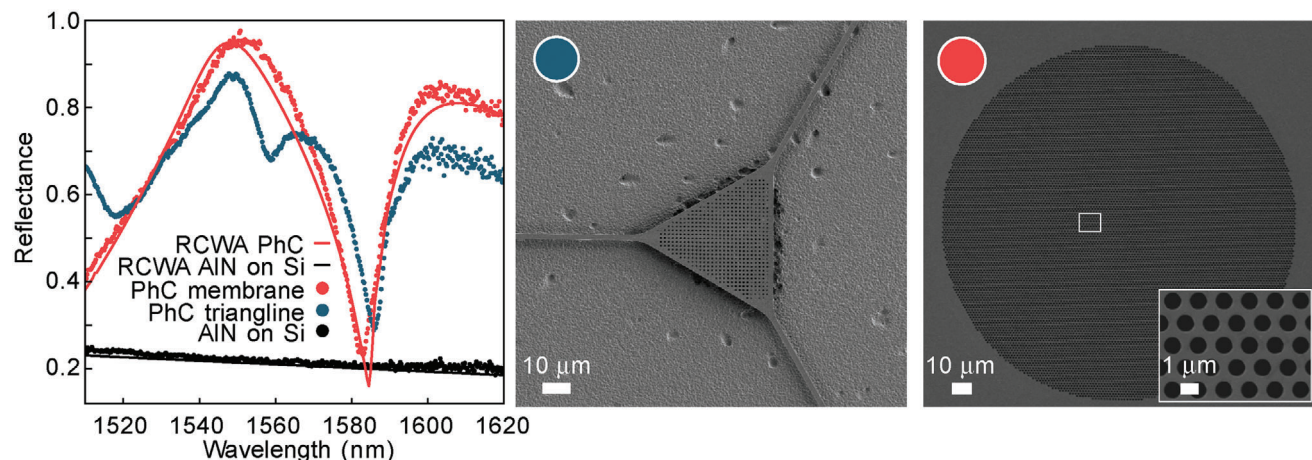
ADVANCED
SCIENCE NEWS

www.advancedsciencenews.com

ADVANCED
MATERIALS

www.advmat.de

Figure 4. Engineering the reflectance of AlN nanomechanical resonators with a hexagonal PhC. Reflectance versus wavelength measurements for an AlN film on a silicon substrate (black), a suspended 180 μm-diameter circular membrane patterned with a PhC (red), and a triangline nanomechanical resonator with a center pad of 60 μm side length patterned with a PhC (blue). Dots are experimental data, solid lines are RCWA simulations for a waist of 6.4 μm. SEM images on the right: Triangline and circular membrane patterned with a PhC. The inset shows the hexagonal PhC pattern.

cavity forming a membrane-in-the-middle-type optomechanical system.[60]

3. Conclusion and Outlook

Table 1 summarizes the parameters of the soft-clamped nanomechanical resonators that we realized in 290 nm-thick crystalline AlN. We calculated the thermal force noise to assess their performance in sensing applications. For example, with the fundamental mode of the long triangline we reach 29.2 aN $(\sqrt{Hz})^{-1}$, which is similar to conventional Si_3N_4-trampolines[53,54] or hierarchically-clamped Si_3N_4 trampolines.[12]

To put crystalline AlN into perspective with other materials used for high-Q_m nanomechanics, we summarize important material properties in **Table 2**. The residual stress of 1.4 GPa of the AlN film is similar to state-of-the-art strained crystalline Si or amorphous Si_3N_4. The AlN film's Q_{int} of 8×10^3 at room temperature is comparable to SiC or Si_3N_4 of similar thickness.[64] The Q_{int} of crystalline materials can, however, surpass the one of amorphous materials at cryogenic temperatures.[19,65] The re-

fractive index of AlN at telecom wavelengths is similar to that of Si_3N_4, but lower than for Si or InGaP. However, we demonstrated that the reflectance of the suspended AlN film can be vastly increased through patterning of a hexagonal PhC. Thanks to its bandgap of 6.2 eV, and wide transparency window from the deep ultraviolet to mid infrared, AlN is an appealing material for low-loss quantum optical devices.[30] The use of AlN for quantum optomechanics devices operating at cryogenic temperatures may therefore improve device performance that is currently hampered by heating due to optical absorption.

A major advantage of using crystalline compared to amorphous materials for nanomechanical resonators is their in-built functionality. For example, crystalline films can be conducting or superconducting, or can exhibit piezoelectricity, provided they lack inversion symmetry. Zincblende or wurtzite crystals like SiC, InGaP and AlN meet the latter requirement. AlN has the largest piezoelectric coupling coefficient[63] among these materials (see Table 2). This has already been exploited in AlN-based GHz nanomechanics, where mechanical excitations, phonons, have been interfaced with superconducting qubits.[24,25] The piezoelectricity of the AlN film would allow, for example, to in situ tune the

Table 1. High-Q_m AlN nanomechanical resonators. f_m and Q_m are experimental values for the mechanical mode eigenfrequency and mechanical quality factor, respectively. The motional mass, m_{eff}, is determined from FEM simulations, and the thermal force noise is calculated as $S_F = \sqrt{4 k_B T m_{eff} \Gamma_m}$.

	Length [μm]	f_m [kHz]	Q_m	$Q_m \times f_{m \, [Hz]}$	m_{eff} [ng]	$\sqrt{S_F}$ [aN/$\sqrt{Hz}$]
1D						
uniform beam	200	1400	5.5×10^5	0.77×10^{12}	0.047	111
Defect in 1D PnC	80	3000	1.5×10^6	4.5×10^{12}	0.35	269
2D						
PhC membrane	180	2000	4.3×10^5	0.86×10^{12}	0.9	657
Short triangline	1700	200	9.4×10^6	1.88×10^{12}	1.22	51.7
Long triangline	4720	87	2.9×10^7	2.5×10^{12}	2.67	29.2
Long triangline	4720	1068	8.7×10^6	9.2×10^{12}	5.27	258.2

2403155 (7 of 11)

**ADVANCED
SCIENCE NEWS**

www.advancedsciencenews.com

**ADVANCED
MATERIALS**

www.advmat.de

Table 2. Materials used for high-Q_m nanomechanics at room temperature. The mechanical properties of the as-grown film are the residual stress σ_{residual}, Young's modulus E, and the strain ϵ. The stress after relaxation, σ_{released}, takes into account Poisson's ratio of the respective material.

	Si_3N_4[61]	SiC[41]	Si[19]	SiC[18]	$In_{0.43}Ga_{0.57}P$[17]	AlN[a]
crystallinity	amorphous	amorphous	diamond cubic	zinc blende	zinc blende	wurtzite
thickness (nm)	20	71	14	337	73	290
Q_{int}	1.4×10^3	5.1×10^3	$(8 \pm 3) \times 10^3$	10^4	8×10^3	8×10^3
n at 1550 nm	1.99	2.56	3.48	2.56	3.15	2.12
σ_{residual} (GPa)	1.14	0.76	1.53 ± 0.11	0.62	0.47	1.43 ± 0.01
E (GPa)	250	223	169	400	80–120	270
ϵ (%)	0.46	0.34	0.85 ± 0.06	0.15	0.49	0.36
σ_{released} (GPa)	0.87	0.62	1	0.51	0.3–0.5	1
piezoelectricity, ϵ_p[b] ($C\,m^{-2}$)	–	–	–	−1.24	−0.23	−1.55
coupling coefficient, k_{piezo} (%)[62]	–	–	–	0.08	0.04	5.6
relative permittivity, ϵ_r	7-8	9.7	11.7	9.7	11.7	10

[a] This work; [b] Wurtzite crystal: uniaxial strain along the c-axis $\epsilon_p = \epsilon_{33}$. zinc blende: uniaxial strain along the $\langle 111 \rangle$ direction $\propto 2\epsilon_{14}/\sqrt{3}$ with an additional contribution from another polar direction.[20,63]

mechanical frequency of the nanomechanical resonator. In our current devices we would expect a frequency tuning coefficient of some kHz V^{-1}, see Supporting Information. Parametric driving could then be used to generate squeezed mechanical states.[66] To make use of the piezoelectricity of the AlN layer, a next step would be to alter the growth and microfabrication of the presented devices such that electrically conductive layers below and above the suspended AlN layer are incorporated.

The presented triangline AlN nanomechanical resonators reached a $Q_m \times f_m$-product close to 10^{13} Hz (see Table 2), sufficient to support a single quantum coherent oscillation at room temperature. We foresee multiple ways to increase device performance further by, for example, using other geometries, such as hexagonal polygon resonators,[67] by etching the defect-rich layer,[18] by reducing the overall thickness of the AlN film, or by operating at low temperatures. In particular, the thickness dependence of strain, intrinsic quality factor, and crystal quality are important parameters that will determine the optimum working point for optoelectromechanical devices made from tensile-strained AlN.[68] In case of 100 nm-thick AlN, one could potentially achieve Q_m of up to 10^{10} and a $Q_m \times f_m$-product of 10^{15} Hz (see Supporting Information), similar to crystalline Si nanomechanical resonators,[19] but then realized in a piezoelectric material. Therefore, nanomechanical resonators from piezoelectric, tensile-strained AlN films hold great promise for interfacing kHz or MHz phonons with superconducting circuits for cavity quantum optomechanics,[22] direct piezoelectric read-out of AlN-based nanomechanical resonators for sensing applications,[69] or coupling of optical, mechanical and electronic degrees of freedom in the same material system.[4]

4. Experimental Section

Growth and Fabrication Details: The AlN film was grown with MOVPE (metal–organic vapor-phase epitaxy, AIXTRON AIX 200/4 RF-S) on a 2-inch 500 μm-thick highly As-doped silicon (111) wafer. A two-step growth process was used, which is optimized to yield compact and very smooth AlN layers (typical AFM RMS $3 \times 3\,\mu m^2 < 0.2$ nm) free from pits.[70] This was achieved by the second growth step which is performed under very low V/III ratio. However, applying such conditions right from the start of

the growth of the layers turns out to result in a lower crystalline quality (as measured in XRD) and in a film that is more tensile-strained. To avoid this undesired feature, the initial 20–40 nm of the AlN film was grown under a much higher V/III ratio. After a thin metallic Al deposition, 20 nm of AlN were grown at a low growth rate with a surface temperature of 1110°C, 100 mbar, and a high V-III ratio of 2500. Then the main AlN layer was grown at 70 mbar and a low V-III ratio of 25 with a surface temperature of 1120°C. During the cooling process, strain was introduced due to the thermal expansion coefficient mismatch between the silicon substrate and the AlN film in addition to tensile strain during growth.[71] XRD measurements of the AlN film indicate a high crystalline quality (for details see Supporting Information).

The fabrication process was started by sputtering a 50 nm SiO_2 hard mask. Subsequently, the pattern of the mechanical resonator in electron-beam resist (UV-60) was defined. Then the pattern was transferred into the hard mask and AlN film in consequent ICP-RIE etching steps with CF_4/CHF_3 and Cl_2/Ar mixtures, respectively. The photoresist was stripped with NMP (Remover 1165), and the sample was cleaned with 1 min HF etching. To release the structure XeF_2 gas was used to selectively etch silicon. A mixture of XeF_2 and N_2 etches silicon isotropically with an etch rate of about 700 nm min^{-1},[72] whereas AlN is inert to XeF_2 at room temperature.[73] During the release process the flux of hydrogen and nitrogen was set to 25 sccm each and the pressure in the chamber was held at 1.2 Torr.

Note that the presented fabrication process was applied on the chip scale. However, both the growth as well as the fabrication process can be scaled up to four inch wafers at least.

Finite Element Simulations: Mechanical Properties: The solid mechanics interface of COMSOL Multiphysics was used for FEM simulations. First a stationary solution was found to determine the redistribution of σ_{residual}. The material parameters used for the simulations are listed in **Table 3**. Then, this static solution entered into the eigenfrequency solver. Finally, the eigenfrequencies and the mechanical displacement field u were extracted, which was further used in the evaluation of Q_D.

The dilution factor D_Q is given by[11]

$$D_Q = 1 + \frac{\langle \Delta W^{(nl)} \rangle}{\langle \Delta W^{(lin)} \rangle} \tag{4}$$

where the time-averaged $<\Delta W^{(lin)}>$ and $<\Delta W^{(nl)}>$ are the linear and non-linear dynamic contributions to the elastic energy of a specific mode shape, respectively.

To calculate D_Q of a crystalline mechanical resonator of thickness h, the general relation between the components of the stress tensor σ_{ij} and

**ADVANCED
SCIENCE NEWS**

www.advancedsciencenews.com

**ADVANCED
MATERIALS**

www.advmat.de

Table 3. Parameters for the FEM simulation. AlN film thickness, h, density ρ, residual stress, $\sigma_{residual}$, intrinsic quality factor, Q_{int}, elastic constants, C_{ij}.[74] We calculate the effective Young's modulus, E, and Poisson's ratio, v, with C_{ij}.

thickness, h [nm]	290
density, ρ [kg m^{-3}]	3255
$\sigma_{residual}$ [GPa]	1.4[a]
Q_{int}	0.8×10^4
C_{11} (GPa)	345
C_{33} (GPa)	395
C_{44} (GPa)	118
C_{12} (GPa)	125
C_{13} (GPa)	120
E (GPa)	283
v	0.287

[a] Note, that $\sigma_{residual}$ differs for the PnC beam simulations and is 1 GPa.

the strain tensor ϵ_{kl} through the elasticity matrix C_{ijlk}, i.e., $\sigma_{ij} = C_{ijlk}\epsilon_{kl}$ is employed. This relation was used to calculate an expression for the time-averaged linear elastic energy $<\Delta W^{(lin)}>$,

$$\left\langle \Delta W^{(lin)} \right\rangle = \frac{h^2}{24} \iint_V \left(\left(\frac{\partial^2 u}{\partial x^2} \right)^2 \left[C_{11} - \frac{C_{13}^2}{C_{33}} \right] + \right.$$

$$+ 2 \frac{\partial^2 u}{\partial x^2} \frac{\partial^2 u}{\partial y^2} \left[C_{12} - \frac{C_{13}C_{23}}{C_{33}} \right] + \left(\frac{\partial^2 u}{\partial y^2} \right)^2 \left[C_{22} - \frac{C_{23}^2}{C_{33}} \right] + \quad (5)$$

$$\left. + 4C_{66} \left(\frac{\partial^2 u}{\partial x \partial y} \right)^2 \right) dV$$

where u is the out-of-plane displacement and the integral V covers the volume of the mechanical resonator geometry. For details with regards to this calculation refer to the Supporting Information.[75,76] In particular, this treatment covers isotropic materials and crystals with cubic, hexagonal and orthorhombic crystal systems. Equation 5 was used to calculate $<\Delta W^{(lin)}>$ for a given eigenmode of the resonator obtained from the FEM simulations. The expression for the calculation of the time-averaged non-linear contribution is related to the total energy of the system and remains unchanged

$$\left\langle \Delta W^{(nl)} \right\rangle = \rho \frac{\omega^2}{2} \iint_V u^2 dV \quad (6)$$

where ω is the eigenfrequency of the particular eigenmode.[77] This expression was also evaluated for a given eigenmode in the FEM simulations. Subsequently, the dilution factor D_Q can be calculated with Equation 4 to obtain $Q_D = D_Q \cdot Q_{int}$.

The motional mass was determined as

$$m_{eff} = \rho \frac{\int_V |u|^2 dV}{|u_{max}|^2} \quad (7)$$

where the entire geometry was integrated over its displacement u, with the maximum displacement u_{max} of that particular eigenmode.

The values of the elastic constants were chosen from the measurements on AlN films[74] with the resulting Young's modulus close to the one determined in this work, 270 GPa. It should be noted that the difference between the reference parameters[74] and the presented AlN film could be

a reason for the small discrepancies of Q_D between the FEM simulation and the experiment.

Simulation: Optical Reflectance: We use a rigorous coupled wave analysis (RCWA) solver, which is available as the Stanford Stratified Structure Solver (S^4) software package.[58] The focused Gaussian beam with a waist was reconstructed as a superposition of plane waves impinging on the PhC.[38] The value of the PhC parameters (a_{PhC}, r_{PhC}) was determined after fabrication via analysis of SEM images. The radius of the PhC holes in the PhC pattern of a circular membrane was $r_{PhC} = 508$ nm and in the case of the triangline it was $r_{PhC} = 502$ nm. The small difference in r_{PhC} results in the slightly different position of the guided mode at 1585 nm observed in Figure 4.

Raman Spectroscopy: Residual stress and strain of the AlN film was evaluated by means of Raman scattering using a confocal Raman microscope at room temperature. A 532 nm laser was used for excitation and was focused down by an objective lens with a magnification of 100× and a numerical aperture of 0.9, leading to an optical spot size of about 300 nm. It was verified that the Raman signal is power-independent and, thus, not affected by a potential heating of the device. Note that the calculation that relates the wavelength of the Raman line to the stress and strain in the AlN film is outlined in the Supporting Information.

Interferometric Characterization Setup: The measurements of AlN resonators were performed at 7×10^{-6} mbar and at room temperature, using optical interferometry driven by a tunable laser with a wavelength of 1550 nm, see **Figure 5**.

The laser beam was reflected off the sample inside a vacuum chamber, and the resulting phase shift was detected using a phase-locked homodyne detector and record its output signal with a spectrum analyzer (SA). The ring-down measurements are performed by resonantly driving the sample with a piezoelectric transducer, switching it off and then recording the decay of the signal.
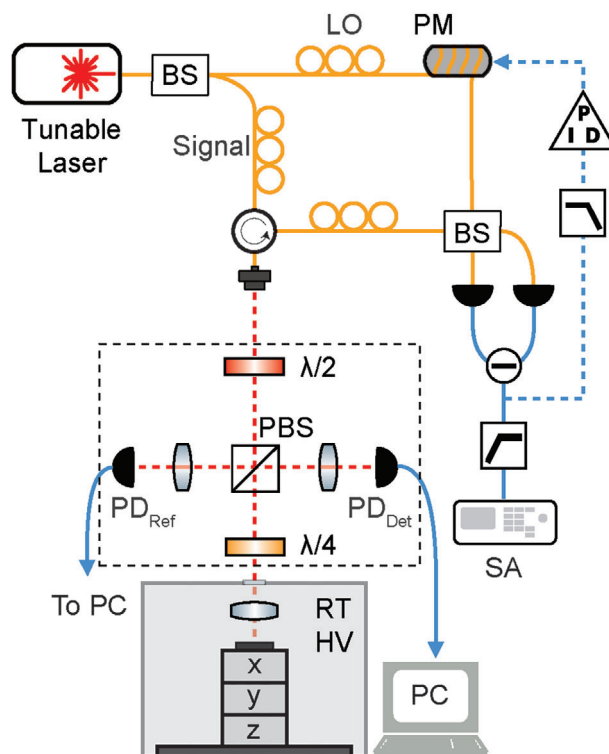

Figure 5. The experimental setup consists of a homodyne detection and a reflectivity measurement (in black-dashed box) parts. The fiber path (yellow solid), free-space (dashed red) and electrical connections (blue).

To measure the reflectance of the samples, the polarization was adjusted with a half-wave plate before the polarizing beam-splitter (PBS) and monitor the incoming laser power via a reference photodetector, PD_{Ref}. The output from PD_{Ref} was fed back to the laser to stabilize the laser power throughout the wavelength sweep. After the PBS, a quarter-wave plate was inserted to detect the reflected intensity with the PD_{Det} photodetector.

Supporting Information

Supporting Information is available from the Wiley Online Library or from the author.

Conflict of Interest

Witlef Wieczorek is a shareholder in WACQT-IP AB.

Author Contributions

A.D. and A.S. grew the samples. A.C., A.J., H.P., and L.R. performed FEM simulations. A.C. and J.C. developed the fabrication process. A.C., A.J., and L.R. fabricated the samples. A.C., A.J., and L.R. performed measurements. A.C., A.J., H.P., L.R., and W.W. analyzed and discussed the data. W.W. supervised the project. All authors contributed to the discussions and preparation of the manuscript.

Data Availability Statement

The data that support the findings of this study are openly available in zenodo at https://zenodo.org/doi/10.5281/zenodo.10679216 , reference number 10679217.

[1] L. Sementilli, E. Romero, W. P. Bowen, *Adv. Funct. Mater.* **2022**, *32*, 2105247.
[2] A. Eichler, *Mater. Quantum Technol.* **2022**, *2*, 043001.
[3] T. Westphal, H. Hepach, J. Pfaff, M. Aspelmeyer, *Nature* **2021**, *591*, 225.
[4] L. Midolo, A. Schliesser, A. Fiore, *Nat. Nanotechnol.* **2018**, *13*, 11.
[5] S. Barzanjeh, A. Xuereb, S. Gröblacher, M. Paternostro, C. A. Regal, E. M. Weig, *Nat. Phys.* **2022**, *18*, 15.
[6] A. Cupertino, D. Shin, L. Guo, P. G. Steeneken, M. A. Bessa, R. A. Norte, *Nature Communications* **2024**, *15*, 4255.
[7] Q. P. Unterreithmeier, T. Faust, J. P. Kotthaus, *Phys. Rev. Lett.* **2010**, *105*, 027205.
[8] P.-L. Yu, T. Purdy, C. Regal, *Phys. Rev. Lett.* **2012**, *108*, 083603.
[9] Y. Tsaturyan, A. Barg, E. S. Polzik, A. Schliesser, *Nat. Nanotechnol.* **2017**, *12*, 776.
[10] A. H. Ghadimi, S. A. Fedorov, N. J. Engelsen, M. J. Bereyhi, R. Schilling, D. J. Wilson, T. J. Kippenberg, *Science* **2018**, *360*, 764.
[11] S. A. Fedorov, N. J. Engelsen, A. H. Ghadimi, M. J. Bereyhi, R. Schilling, D. J. Wilson, T. J. Kippenberg, *Phys. Rev. B* **2019**, *99*, 054107.
[12] M. J. Bereyhi, A. Beccari, R. Groth, S. A. Fedorov, A. Arabmoheghi, T. J. Kippenberg, N. J. Engelsen, *Nat. Commun.* **2022**, *13*, 3097.
[13] D. Shin, A. Cupertino, M. H. de Jong, P. G. Steeneken, M. A. Bessa, R. A. Norte, *Adv. Mater.* **2022**, *34*, 2106248.
[14] D. Høj, F. Wang, W. Gao, U. B. Hoff, O. Sigmund, U. L. Andersen, *Nat. Commun.* **2021**, *12*, 5766.
[15] G. D. Cole, P.-L. Yu, C. Gärtner, K. Siquans, R. Moghadas Nia, J. Schmöle, J. Hoelscher-Obermaier, T. P. Purdy, W. Wieczorek, C. A. Regal, M. Aspelmeyer, *Appl. Phys. Lett.* **2014**, *104*, 130788.
[16] M. Bückle, V. C. Hauber, G. D. Cole, C. Gärtner, U. Zeimer, J. Grenzer, E. M. Weig, *Appl. Phys. Lett.* **2018**, *113*, 594332.
[17] S. K. Manjeshwar, A. Ciers, F. Hellman, J. Bläsing, A. Strittmatter, W. Wieczorek, *Nano Lett.* **2023**, *23*, 5076.
[18] E. Romero, V. M. Valenzuela, A. R. Kermany, L. Sementilli, F. Iacopi, W. P. Bowen, *Phys. Rev. Appl.* **2020**, *13*, 044007.
[19] A. Beccari, D. A. Visani, S. A. Fedorov, M. J. Bereyhi, V. Boureau, N. J. Engelsen, T. J. Kippenberg, *Nat. Phys.* **2022**, *18*, 436.
[20] V. Cimalla, J. Pezoldt, O. Ambacher, *J. Phys. D: Appl. Phys.* **2007**, *40*, S19.
[21] K. Brueckner, F. Niebelschuetz, K. Tonisch, C. Foerster, V. Cimalla, R. Stephan, J. Pezoldt, T. Stauden, O. Ambacher, M. Hein, *Phys. Status Solidi A* **2011**, *208*, 357.
[22] B. M. Brubaker, J. M. Kindem, M. D. Urmey, S. Mittal, R. D. Delaney, P. S. Burns, M. R. Vissers, K. W. Lehnert, C. A. Regal, *Phys. Rev. X* **2022**, *12*, 021062.
[23] Y. Seis, T. Capelle, E. Langman, S. Saarinen, E. Planz, A. Schliesser, *Nat. Commun.* **2022**, *13*, 1507.
[24] A. D. O'Connell, M. Hofheinz, M. Ansmann, R. C. Bialczak, M. Lenander, E. Lucero, M. Neeley, D. Sank, H. Wang, M. Weides, et al., *Nature* **2010**, *464*, 697.
[25] M. Mirhosseini, A. Sipahigil, M. Kalaee, O. Painter, *Nature* **2020**, *588*, 599.
[26] H. Morkoç, *Handbook of Nitride Semiconductors and Devices*, Wiley-VCH, Weinheim **2008**.
[27] M. Kneissl, J. Rass, *III-Nitride Ultraviolet Emitters: Technology and Applications*, Springer International, Cham **2016**.
[28] Y. Xue, H. Wang, N. Xie, Q. Yang, F. Xu, B. Shen, J.-j. Shi, D. Jiang, X. Dou, T. Yu, et al., *J. Phys. Chem. Lett.* **2020**, *11*, 2689.
[29] K. Taylor, C. Lenie, *J. Electrochem. Soc.* **1960**, *107*, 308.
[30] X. Liu, A. W. Bruch, H. X. Tang, *Adv. Opt. Photonics* **2023**, *15*, 236.
[31] A. Cleland, M. Pophristic, I. Ferguson, *Appl. Phys. Lett.* **2001**, *79*, 2070.
[32] K. Brueckner, C. Forster, K. Tonisch, V. Cimalla, O. Ambacher, R. Stephan, K. Blau, M. Hein, in *2005 European Microwave Conference*, IEEE, Paris, France **2005**.

**ADVANCED
SCIENCE NEWS**

www.advancedsciencenews.com

**ADVANCED
MATERIALS**

www.advmat.de

[33] W. H. P. Pernice, C. Xiong, C. Schuck, H. Tang, *Appl. Phys. Lett.* **2012**, *100*, 23786.

[34] M. Ghasemi Baboly, S. Alaie, C. Reinke, I. El-Kady, Z. C. Leseman, *J. Appl. Phys.* **2016**, *120*, 143780.

[35] L. Sang, M. Liao, X. Yang, H. Sun, J. Zhang, M. Sumiya, B. Shen, *Sci. Technol. Adv. Mater.* **2020**, *21*, 515.

[36] M. Placidi, J. Moreno, P. Godignon, N. Mestres, E. Frayssinet, F. Semond, C. Serre, *Sens. Actuators, A* **2009**, *150*, 64.

[37] S. Fan, J. D. Joannopoulos, *Phys. Rev. B* **2002**, *65*, 235112.

[38] S. Kini Manjeshwar, K. Elkhouly, J. M. Fitzgerald, M. Ekman, Y. Zhang, F. Zhang, S. M. Wang, P. Tassin, W. Wieczorek, *Appl. Phys. Lett.* **2020**, *116*, 264001.

[39] G. Enzian, Z. Wang, A. Simonsen, J. Mathiassen, T. Vibel, Y. Tsaturyan, A. Tagantsev, A. Schliesser, E. S. Polzik, *Opt. Express* **2023**, *31*, 13040.

[40] F. Zhou, Y. Bao, J. J. Gorman, J. R. Lawall, *Laser Photonics Rev.* **2023**, *17*, 2300008.

[41] M. Xu, D. Shin, P. M. Sberna, R. van der Kolk, A. Cupertino, M. A. Bessa, R. A. Norte, *Adv. Mater.* **2023**, *36*, 2306513.

[42] R. Liu, F. Ponce, A. Dadgar, A. Krost, *Appl. Phys. Lett.* **2003**, *83*, 860.

[43] N. Mante, S. Rennesson, E. Frayssinet, L. Largeau, F. Semond, J. Rouvière, G. Feuillet, P. Vennéguès, *J. Appl. Phys.* **2018**, *123*, 124215.

[44] M. Mastro, C. Eddy Jr, D. Gaskill, N. Bassim, J. Casey, A. Rosenberg, R. Holm, R. Henry, M. Twigg, *J. Cryst. Growth* **2006**, *287*, 610.

[45] G. Callsen, M. Wagner, J. Reparaz, F. Nippert, T. Kure, S. Kalinowski, A. Hoffmann, M. Ford, M. Phillips, R. Dalmau, et al., *Phys. Rev. B* **2014**, *90*, 205206.

[46] P. Li, J.-Y. Ou, G. Z. Mashanovich, J. Yan, *Opt. Express* **2022**, *30*, 27092.

[47] Y. S. Klaß, J. Doster, M. Bückle, R. Braive, E. M. Weig, *Appl. Phys. Lett.* **2022**, *121*, 2834205.

[48] G. Zeng, W. Sun, R. Song, N. Tansu, B. A. Krick, *Sci. Rep.* **2017**, *7*, 14126.

[49] S. Parsons, *Acta Crystallogr. Sect. D: Biol. Crystallogr.* **2003**, *59*, 1995.

[50] S. Schmid, K. Jensen, K. Nielsen, A. Boisen, *Phys. Rev. B* **2011**, *84*, 165307.

[51] A. H. Safavi-Naeini, O. Painter, *Opt. Express* **2010**, *18*, 14926.

[52] Y. Tsaturyan, Ph.D. Thesis, University of Copenhagen, Copenhagen **2019**.

[53] R. A. Norte, J. P. Moura, S. Gröblacher, *Phys. Rev. Lett.* **2016**, *116*, 147202.

[54] C. Reinhardt, T. Müller, A. Bourassa, J. C. Sankey, *Phys. Rev. X* **2016**, *6*, 021001.

[55] S. A. Fedorov, A. Beccari, N. J. Engelsen, T. J. Kippenberg, *Phys. Rev. Lett.* **2020**, *124*, 025502.

[56] S. A. Fedorov, A. Beccari, A. Arabmoheghi, D. J. Wilson, N. J. Engelsen, T. J. Kippenberg, *Optica* **2020**, *7*, 1609.

[57] M. Aspelmeyer, T. J. Kippenberg, F. Marquardt, *Rev. Mod. Phys.* **2014**, *86*, 1391.

[58] V. Liu, S. Fan, *Comput. Phys. Commun.* **2012**, *183*, 2233.

[59] S. K. Manjeshwar, A. Ciers, J. Monsel, H. Pfeifer, C. Peralle, S. M. Wang, P. Tassin, W. Wieczorek, *Opt. Express* **2023**, *31*, 30212.

[60] C. Gärtner, J. P. Moura, W. Haaxman, R. A. Norte, S. Gröblacher, *Nano Lett.* **2018**, *18*, 7171.

[61] M. J. Bereyhi, A. Beccari, S. A. Fedorov, A. H. Ghadimi, R. Schilling, D. J. Wilson, N. J. Engelsen, T. J. Kippenberg, *Nano Lett.* **2019**, *19*, 2329.

[62] M. Rais-Zadeh, V. J. Gokhale, A. Ansari, M. Faucher, D. Théron, Y. Cordier, L. Buchaillot, *J. Microelectromech. Syst.* **2014**, *23*, 1252.

[63] K. Hübner, *Phys. Status Solidi B* **1973**, *57*, 627.

[64] L. G. Villanueva, S. Schmid, *Phys. Rev. Lett.* **2014**, *113*, 227201.

[65] Y. Tao, J. M. Boss, B. Moores, C. L. Degen, *Nat. Commun.* **2014**, *5*, 3638.

[66] D. Rugar, P. Grütter, *Phys. Rev. Lett.* **1991**, *67*, 699.

[67] M. J. Bereyhi, A. Arabmoheghi, A. Beccari, S. A. Fedorov, G. Huang, T. J. Kippenberg, N. J. Engelsen, *Phys. Rev. X* **2022**, *12*, 021036.

[68] A. Ciers, A. Jung, J. Ciers, L. Nindito, H. Pfeifer, A. Dadgar, A. Strittmatter, W. Wieczorek, *Manuscr. Preparat.* **2024**.

[69] H. Mahmoodi Nasrabadi, M. Mahdavi, M. Soleymaniha, S. Moheimani, *Rev. Sci. Instrum.* **2022**, *93*, 2848972.

[70] A. Dadgar, A. Krost, J. Christen, B. Bastek, F. Bertram, A. Krtschil, T. Hempel, J. Bläsing, U. Haboeck, A. Hoffmann, *J. Cryst. Growth* **2006**, *297*, 306.

[71] S. Raghavan, J. M. Redwing, *J. Cryst. Growth* **2004**, *261*, 294.

[72] H. Winters, J. Coburn, *Appl. Phys. Lett.* **1979**, *34*, 70.

[73] M. Watanabe, Y. Mori, T. Ishikawa, H. Sakai, T. Iida, K. Akiyama, S. Narita, K. Sawabe, K. Shobatake, *J. Vac. Sci. Technol. A: Vac., Surf., Films* **2005**, *23*, 1647.

[74] K. Tsubouchi, K. Sugai, N. Mikoshiba, in *1981 Ultrasonics Symposium*, IEEE, **1981**, pp. 375–380.

[75] A. Ciers, A. Jung, J. Ciers, L. R. Nindito, H. Pfeifer, A. Dadgar, A. Strittmater, W. Wieczorek, *Zenodo* **2024**, https://zenodo.org/doi/10.5281/zenodo.10679216.

[76] We supply a short Mathematica script for these calculations on linear contribution to the elastic energy for an anisotropic material.[75]

[77] S. Fedorov, Ph.D. Thesis, EPFL, Lausanne **2021**.